ELSEVIER

Sensors and Actuators B 53 (1998) 76–90

SENSORS AND ACTUATORS B CHEMICAL

Gas sensing and structural properties of variously pretreated nanopowder tin (IV) oxide samples

Martin J. Willett [a,*], Vasilis N. Burganos [b], Christos D. Tsakiroglou [b], Alkiviades C. Payatakes [b]

[a] *City Technology Ltd, City Technology Centre, Walton Road, Portsmouth, Hants. PO6 1SZ, UK*
[b] *Institute Of Chemical Engineering and High Temperature Chemical Processes—Foundation For Research and Technology, Hellas (ICE/HT-FORTH) PO Box 1414, GR 26500, Patras, Greece*

Received 2 March 1998; accepted 27 July 1998

Abstract

The correlation between the gas sensing properties and the pore structure of pure nanopowder SnO_2 samples subjected to varying degrees of thermal pretreatment has been investigated. It is shown that both the intrinsic air resistance and the sensitivity to reducing gases are generally more dependent upon operating temperature than the degree of pretreatment. Nevertheless, there is evidence for a correlation between the porosity and the observed gas sensitivities of samples which have not undergone significant grain growth. It is concluded that under fixed operating conditions, the pore structure of the oxide strongly influences the observed gas sensitivity in such samples.

Keywords: Tin (IV) oxide; SnO_2; Nanopowder; Gas sensors; Porosity

1. Introduction

Tin (IV) oxide, SnO_2, is commonly used as the basis of commercial sensors for the detection of low levels of reducing gases. Numerous studies into the gas sensing characteristics of the oxide have been reported in which attempts have been made to correlate various properties of the material with the observed responses to gases [1–3]. However, there has been comparatively little effort devoted to modelling the pore structure of the material in order to relate this important aspect to the gas sensing behaviour. Such information is of particular value in the case of highly porous structures such as those derived from nanopowders. The high surface to bulk ratios in these materials can result in particularly high gas sensitivities due to the key role played by gas-surface interactions in the detection process. However, the requirement for reactant species to access surfaces deep inside a highly porous structure also implies that the nature of the porosity in the material may strongly influence the observed behaviour. It is the purpose of this study to provide data correlating the nature of the pore structure in nanopowder SnO_2 (n-SnO_2) with the gas sensing properties demonstrated by the oxide. In addition to attempting to provide explanations for the observed behaviour, the results of such studies may suggest ways in which the materials might be modified in order to produce improved sensors.

Mercury porosimetry has been shown to provide reliable structure information for a wide range of porous materials, including ceramics in unconsolidated and consolidated form [4–6]. The interpretation of the mercury intrusion/retraction curves is usually made through a model of the pore structure and has been significantly improved with the use of computer-aided porosimetry simulators [7]. The latter have contributed to the elucidation and quantification of critical structural features, such as pore connectivity, pore-chamber and pore-throat size distribution, spatial correlation of pore sizes and pore surface microroughness [7–9]. In general, the pore space of packs of spheres [6,10,11] consists of pore-chambers (wide void spaces left between neighbouring particles touching each other) and pore-throats (narrow openings connecting adjacent chambers). Theoretical analyses have shown that the

* Corresponding author. Tel.: +44 1705 325511; fax: +44 1705 386611; e-mail: mwillett@citytech.co.uk

0925-4005/98/$ - see front matter
PII S0925-4005(98)00291-3

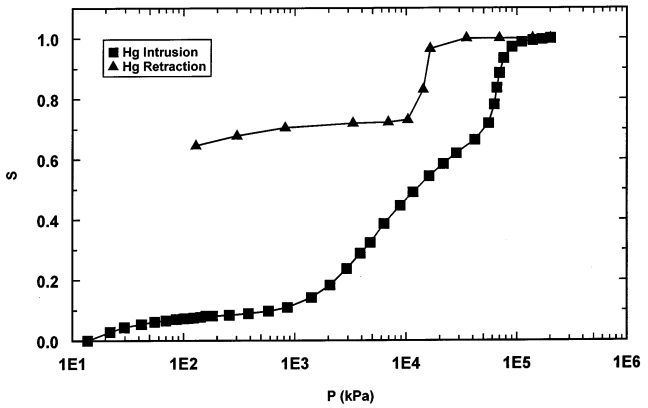

Fig. 1. Experimental mercury intrusion/retraction curves for an untreated n-SnO_2 disc sample.

pressure levels required for mercury intrusion in a pore network are decided by throat-sizes and the pressure region for mercury retraction from the network is specified by chamber sizes, whereas the chamber-size to throat-size aspect ratio influences the residual mercury saturation that is trapped at the end of the retraction stage [7].

Nitrogen adsorption-desorption isotherms are widely used in the characterisation of microporous solids [12]. Pore network models based on percolation theory [13,14], molecular models of mean-field theory [15] as well as methods of molecular dynamics [16] have been adopted for the simulation of nitrogen condensation/evaporation in nano-pores and for the interpretation of experimental results. In addition to the specific surface area, the pore-size distribution and the pore space connectivity, information about the surface fractal properties of porous materials also can be extracted from nitrogen adsorption data at low vapour pressures [17].

Although these powerful methods offer the means to investigate the pore structure of materials, a sample format simultaneously satisfying the requirements of both gas sensitivity and porosimetry is required. Practical SnO_2 sensor structures typically comprise sintered oxide masses or films intimately attached to a heated substrate. Porosimetry measurements do not allow the properties of the oxide to be readily distinguished from those attributable to the remainder of such structures and are therefore unable to provide the required parametric inputs to the pore model. An appropriate compromise was achieved by compacting the SnO_2 into self-supporting discs and simulating the thermal pretreatment typically employed in sensor construction by firing the samples at a range of temperatures.

2. Experimental

2.1. Sample preparation and physical characterisation

Tin (IV) oxide (median particle size ≈ 20 nm) was produced at the Technical University of Clausthal (TUC) via a laser ablation technique described elsewhere [18]. Powder was pressed into discs 30 mm in diameter and 2 mm thick, which were then fired for 2 h in air at 400, 600, 800, 1000 or 1200°C. Unfired pressed discs were supplied as well, whilst identically fired but unpressed powder was also used for mercury porosimetry measurements. The powders were subjected to X-ray crystallographic analysis by TUC whilst electron micrographs of the pressed discs and estimated mean particle size data were supplied by Fraunhofer Institut für Biomedizinische Technik (FhG-IBMT).

2.2. Mercury porosimetry experiments

Capillary pressure curves of the SnO_2 disc samples were measured with stepwise mercury intrusion/retraction experiments performed on a 9305 Mercury Porosimeter (Micromeritics Ltd) operating in the pres-

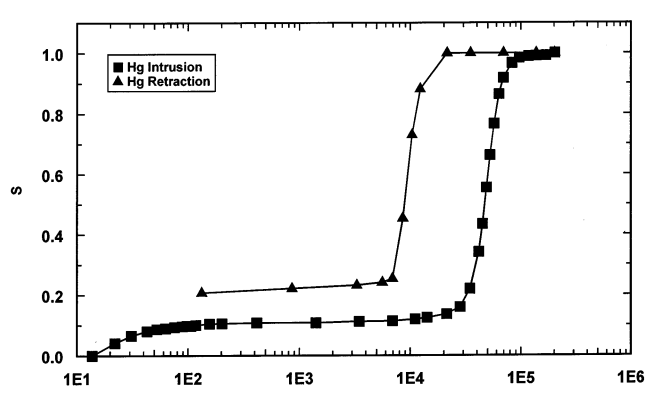

Fig. 2. Experimental mercury intrusion/retraction curves for a n-SnO_2 disc sample pretreated at 400°C.

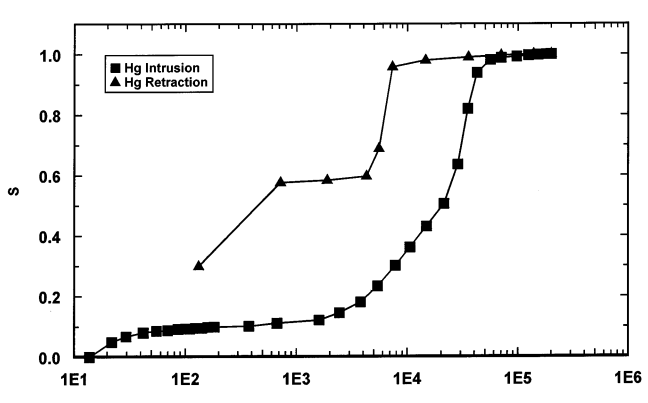

Fig. 3. Experimental mercury intrusion/retraction curves for a n-SnO_2 disc sample pretreated at 600°C.

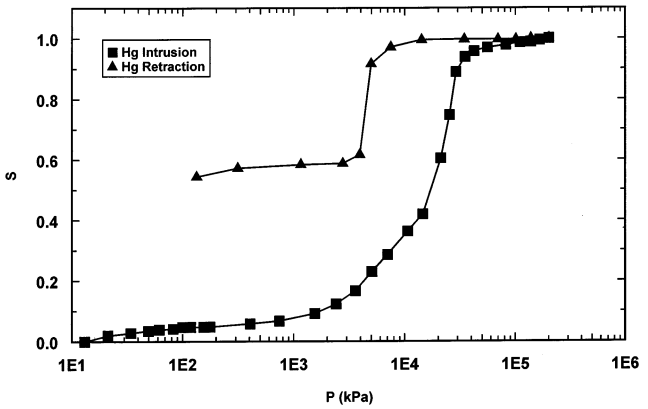

Fig. 4. Experimental mercury intrusion/retraction curves for a n-SnO_2 disc sample pretreated at 800°C.

sure region 10 kPa $< P <$ 200 MPa. Compressibility effects on the mercury and the glass holder assembly were removed from experimental measurements using data from blank runs without samples [19]. The pore volume V_m and the porosity φ were calculated from the mercury intrusion volume at the maximum feasible external pressure (200 MPa). The specific surface area A_m of the samples was obtained through integrating the mercury intrusion curve, according to the relationship

$$A_m = \frac{V_m}{\gamma \cos \theta_I} \int_0^1 PdS \quad (1)$$

where P is the applied pressure, S is the mercury saturation, γ is the mercury/air interfacial tension and θ_I is the mercury intrusion contact angle. The parameter values $\gamma = 0.48$ N m^{-1} and $\theta_I = 40°$ were used [20]. The quantity $4V_m/A_m$ gives the mean intercept length of the void space of the sample and provides a good measure of the mean pore diameter.

The conventional method of analysis of mercury porosimetry data was used for the determination of the pore-size distributions of samples [21]. In this approach, the pore space is represented with a bundle of parallel cylindrical capillary tubes of equal length. Based on the simplified Young–Laplace equation for cylindrical capillaries, the capillary pressure P_c encountered by mercury at the pore entrance is given by

$$P_c = \frac{2\gamma \cos \theta_I}{R} \quad (2)$$

where R is the capillary throat radius. An equivalent cylindrical pore radius distribution was obtained by differentiation of the mercury intrusion/retraction curves. The bundle tube model was used for determining the throat radius distribution from the intrusion curve, whilst the chamber radius distribution was obtained from the retraction curve (ignoring any contact angle hysteresis; $\theta_I = \theta_R = 40°$). With the use of the unconstrained Marquardt non-linear parameter estimation method [22], each experimental throat-radius distribution was fitted to a bimodal distribution function of the form

$$f_t(R) = c_t f_{t1}(R) + (1 - c_t) f_{t2}(R) \quad (3)$$

where f_{t1}, f_{t2} are lognormal component distributions with contribution fractions c_t and $(1 - c_t)$, respectively. The same procedure was also followed for the chamber-radius distributions.

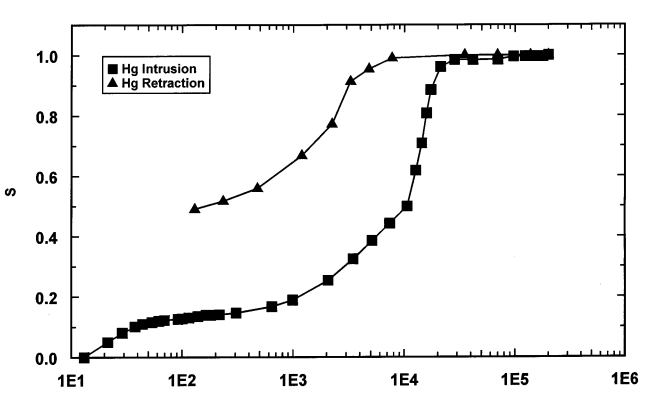

Fig. 5. Experimental mercury intrusion/retraction curves for a n-SnO_2 disc sample pretreated at 1000°C.

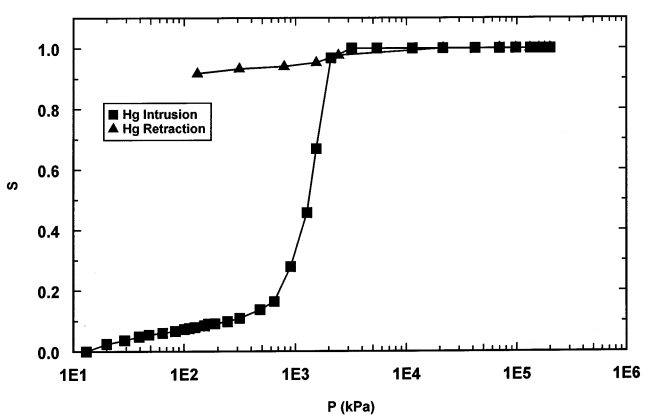

Fig. 6. Experimental mercury intrusion/retraction curves for a n-SnO_2 disc sample pretreated at 1200°C.

2.3. Baseline resistance and gas sensitivity measurements

Heatable alumina substrates (Platfilm E11340, Rosemount Ltd) mounted on TO5 headers were employed in the gas sensitivity measurements. These devices comprise a Pt resistance heater on the lower surface with a pair of platinum pads on the upper face, allowing the electrical resistance of suitably mounted materials to be measured at a variety of temperatures. Disc samples a few mm across were attached to the upper face using A1644 gold paste (Engelhard Clal Ltd), which was thermally cured by a brief ($\sim$1 min) excursion to $\sim$500°C. Contact resistances were assumed to be negligible in comparison with the inherent resistivities of the samples and any variation in the effective electrode separation of the different samples was also neglected. At least four

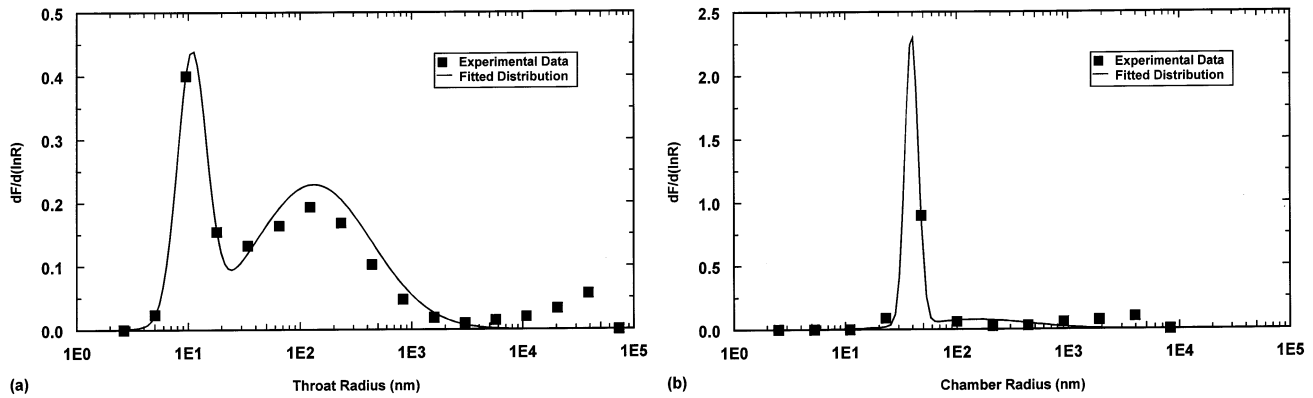

Fig. 7. Throat (a) and chamber (b) size distributions for an untreated n-SnO_2 disc sample.

samples of each disc were mounted and tested during the course of this study, although some devices failed due to cracking of the fragile oxide disc.

Gas exposures were performed by mounting the sensors in a sealed test chamber ($110 \times 110 \times 75$ mm) through which gases were flowed at a rate of 500 ml min^{-1}. A model 2000 gas blender (Environics Ltd) was used to produce the required concentrations of reducing gases in air from pressurised cylinders (BOC Ltd), diluted to standard concentrations of 1000 ppm for CO and H_2 and 1097 ppm for CH_4. Additional tests between 50 ppm and 1.5% CH_4 were also undertaken. Source gases were supplied ready-dried and so all data described here was obtained at a nominal 0% RH level.

Up to 12 devices were simultaneously tested in the chamber. These were powered by a PPS1326 constant current supply (Amrel Ltd) and SnO_2 resistances were monitored using a 2000 digital multimeter (Keithley Ltd) capable of reading up to 10^8 Ω, multiplexed via a 7001 switch (Keithley Ltd). Data acquisition and sensor heater currents were controlled via Testpoint software (Capital Equipment) addressing IEEE488 interfaces on the relevant hardware. Gas sensitivities $\$_{Gas}$ were defined using the formula

$$\$_{Gas} = \frac{G_{Gas} - G_{Air}}{G_{Air}} \quad (4)$$

where G_{Gas} is the sample conductance (Ω^{-1}) in the relevant atmosphere.

3. Description of results

3.1. Pore structure

Table 1 shows that the surface area of the material falls monotonically with increasing pretreatment temperature and although the estimated particle size increases rapidly above 600°C, there is no evidence for significant grain growth below this temperature. The colour of the pressed discs also showed significant variations, changing from mid-brown in the as-prepared form to pure white at pretreatment temperatures above 800°C.

Figs. 1–6 illustrate the mercury intrusion/retraction curves obtained for the variously pretreated discs. The tail of the mercury intrusion curves at pressures below 1 MPa reflects the filling of macroroughness of the sample boundaries corresponding to a fraction of measured porosity from 0.05 to 0.15 and can be ignored in the rest of the analysis. Two distinct regions may be identified along each mercury intrusion curve: (i) an abrupt section with a very

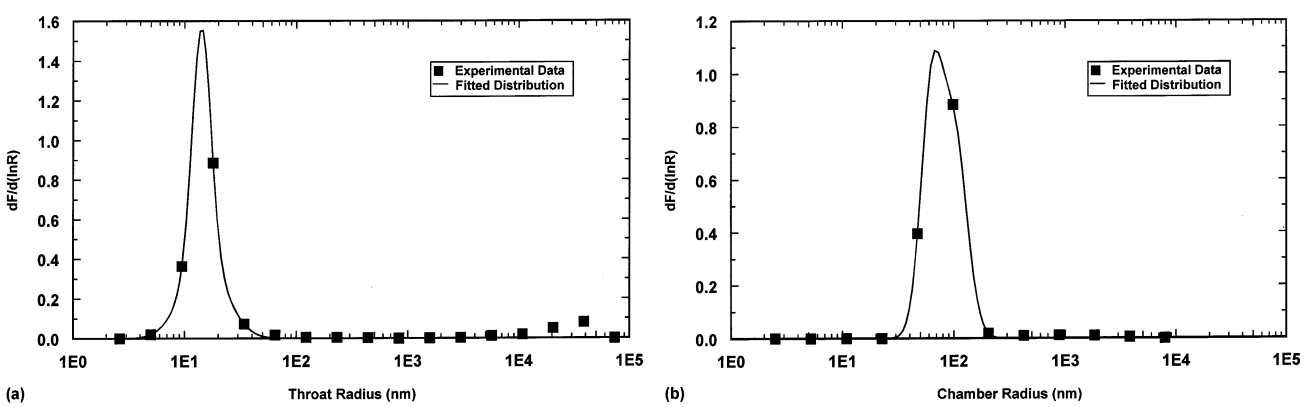

Fig. 8. Throat (a) and chamber (b) size distributions for a n-SnO_2 disc sample pretreated at 400°C.

Table 1
Porosity parameters of variously pretreated n-SnO_2 pressed disc samples

Pretreatment temperature (°C)	Particle size (nm)	Porosity	Pore volume ($cm^3\ g^{-1}$)	Surface area ($m^2\ g^{-1}$)	Mean pore diameter (nm)	Most probable throat sizes (bimodal distribution) (nm)		Most probable chamber sizes (bimodal distribution) (nm)	
						Component 1	Component 2	Component 1	Component 2
Pressed discs									
Untreated	20–30	0.775	0.514	40.6	50.6	11.3	270.6	39.8	285.8
400	30	0.544	0.260	32.0	32.5	14.4	16.6	65.2	105.2
600	30	0.754	0.475	27.3	69.6	24.4	161.2	86.8	2345.0
800	50	0.792	0.419	21.9	76.5	36.2	303.4	179.0	149.7
1000	100	0.776	0.432	12.4	139.4	51.3	1941.6	304.0	3090.1
1200	500	0.704	0.297	1.0	1188.0	544.7	748.0	—	—
As % of untreated sample value									
Untreated	100	100.0	100.0	100.0	100	—	—	—	—
400	120	70.2	50.6	78.8	64	—	—	—	—
600	120	97.3	92.4	67.2	138	—	—	—	—
800	200	102.2	81.5	53.9	151	—	—	—	—
1000	400	100.1	84.0	30.5	276	—	—	—	—
1200	2000	90.8	57.8	2.5	2348	—	—	—	—
Precursor powders									
Untreated	—	0.867	2.07	51.8	—	—	—	—	—
400	—	0.859	1.72	37.9	—	—	—	—	—
600	—	0.801	1.48	30.2	—	—	—	—	—
800	—	0.824	1.51	24.1	—	—	—	—	—
1000	—	0.859	1.38	13.9	—	—	—	—	—

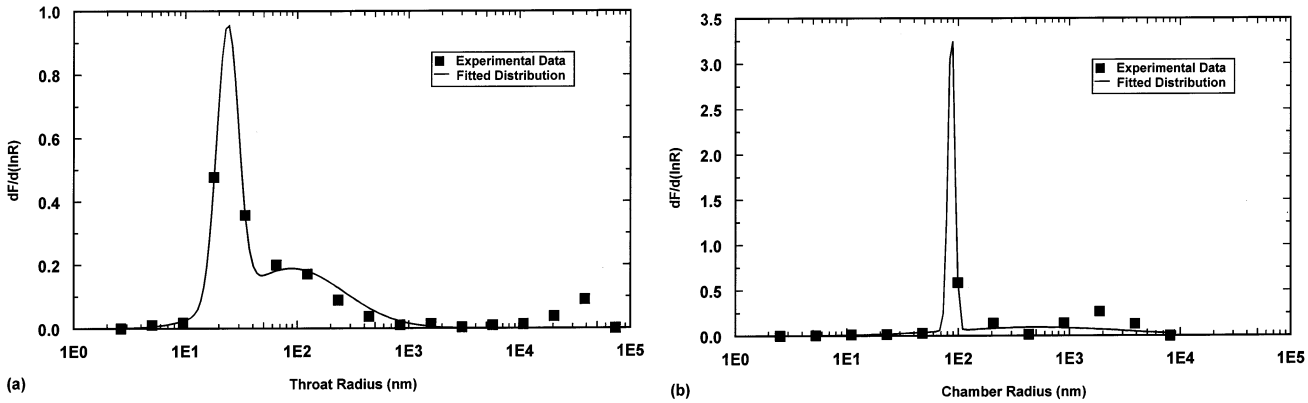

Fig. 9. Throat (a) and chamber (b) size distributions for a n-SnO_2 disc sample pretreated at 600°C.

large slope at high pressures; and (ii) a region with much smaller slope extending over a wide region of relatively low pressures. This type of capillary behaviour can be interpreted in terms of dual pore networks, yielding the throat and chamber size distributions shown in Figs. 7–12 where dF is the fraction of the total pore volume corresponding to pores with radii in the interval $(R, R+\mathrm{d}R)$. Fitting a bimodal density function to these data yields the most probable throat and chamber sizes shown in Table 1. Sintering at 400°C appears to eliminate the second throat size distribution peak found in untreated samples, whereas sintering at further elevated temperatures restores it gradually and, finally, shifts the throat sizes to larger values. Sintering at 1200°C results in very large chamber sizes that cannot be emptied from mercury and, consequently, cannot be determined by mercury porosimetry.

Fig. 13 shows parameters from Table 1 normalised with respect to the properties of unfired discs. For clarity, data pertaining to the untreated samples have been plotted at a pretreatment temperature of 20°C throughout this work.

3.2. Electrical data

Fig. 14 shows typical baseline characteristics of the disc samples obtained as the operating temperature was increased under an atmosphere of dry air. All samples demonstrated qualitatively similar behaviour and there was comparatively little variation between the initial run and subsequent tests with the same sample. As the temperature increased from ambient to $\sim$200°C the oxide resistance fell sharply, before rising more gradually between $\sim$200 and $\sim$380°C. Further increases in temperature produced a monotonic fall in resistance. The first point of inflection occurred at $\sim$200°C irrespective of pretreatment conditions, but there was some evidence that the intermediate peak increasingly shifted towards lower operating temperatures for oxides previously subjected to higher conditioning temperatures.

The absolute resistance values are subject to some uncertainty due to the variation in the sample size and contact spacing in the different devices. It is nevertheless clear from Table 2 that the air resistance of pretreated samples measured at any operating temperature increases steadily with the severity of the ther-

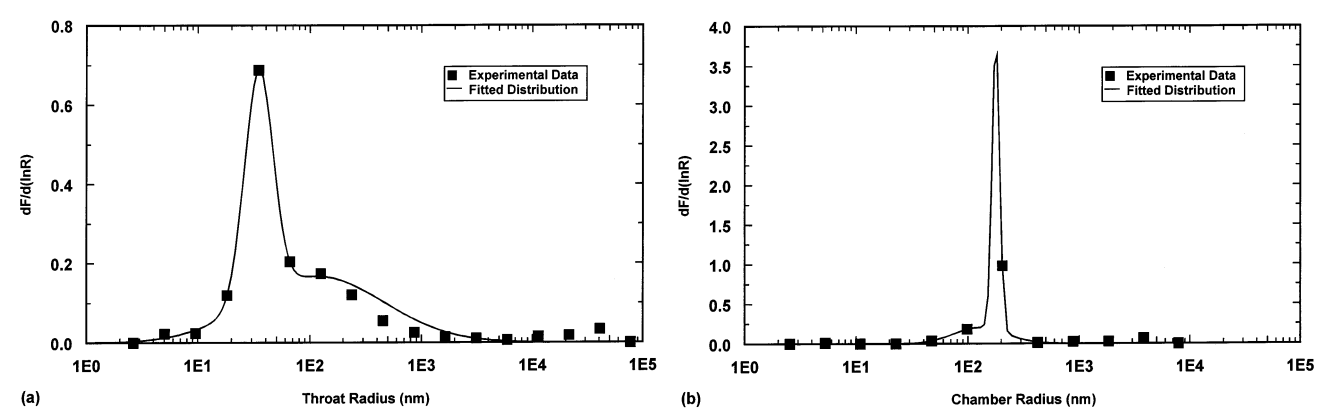

Fig. 10. Throat (a) and chamber (b) size distributions for a n-SnO_2 disc sample pretreated at 800°C.

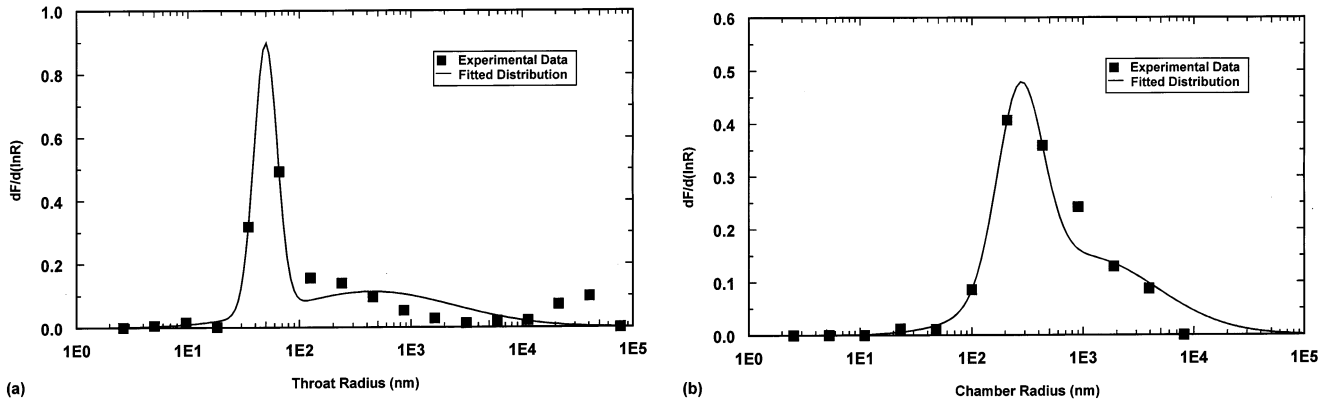

Fig. 11. Throat (a) and chamber (b) size distributions for a n-SnO_2 disc sample pretreated at 1000°C.

mal pretreatment. The estimated activation energies (E_{Act}) of the processes controlling the resistance variations in the low (< 150°C) and high (> 350°C) temperature regions also increased with pretreatment. In all cases, however, unfired samples demonstrated behaviour intermediate between that observed for 400 and 800°C pretreated materials.

Table 3 summarises the mean gas sensitivities of the variously pretreated materials as a function of operating temperature at the standard concentrations of CH_4, CO and H_2 employed. Figs. 15–17 show these data plotted together with polynomial curves fitted using a standard software package (FigP, Biosoft Ltd). For each gas, the sensitivity distributions as a function of operating temperature were qualitatively similar for all samples except those pretreated at 1200°C, which invariably had negligible sensitivities. In the case of CO, there was some evidence for a secondary sensitivity peak at low temperatures (~ 150°C), but no attempt has been made to analyse this effect in detail here.

The peak sensitivities and the operating temperatures at which they occurred were estimated from these curves, yielding the values shown in Table 4. In view of the range of behaviour observed for nominally identical samples, the variations in operating temperature of the maximum sensitivity as a function of pretreatment conditions were not considered significant. Thus, the results may be expressed in terms of the mean values for samples pretreated at or below 1000°C, giving optima of 536 ± 10°C in CH_4, 406 ± 4°C in CO and 401 ± 10°C in H_2.

In order to clarify further the relative magnitudes of the effects due to operating and pretreatment temperature variations, the peak gas sensitivities were normalised with respect to the values demonstrated by the unfired samples, producing mean sensitivity ratios as shown in Table 4 and Fig. 18. The air baseline data have also been expressed in this normalised form; these values have been averaged over all operating temperatures. Despite the relatively high level of uncertainty in the mean values, a rapid increase in the baseline ratio as a function of pretreatment temperature above 600°C is clear.

In subsequent experiments intended to study the

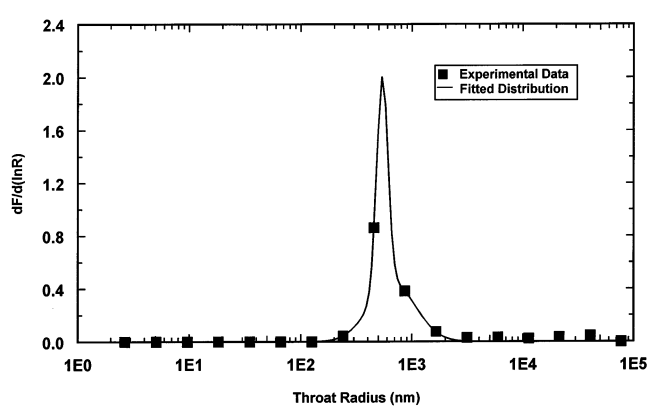

Fig. 12. Throat size distributions for a n-SnO_2 disc sample pretreated at 1200°C.

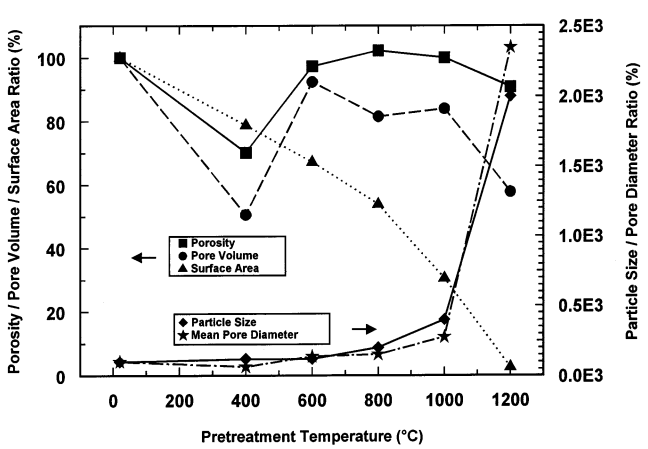

Fig. 13. Morphological and porosity parameter ratios of variously pretreated n-SnO_2 disc samples (with respect to untreated samples) as a function of pretreatment temperature.

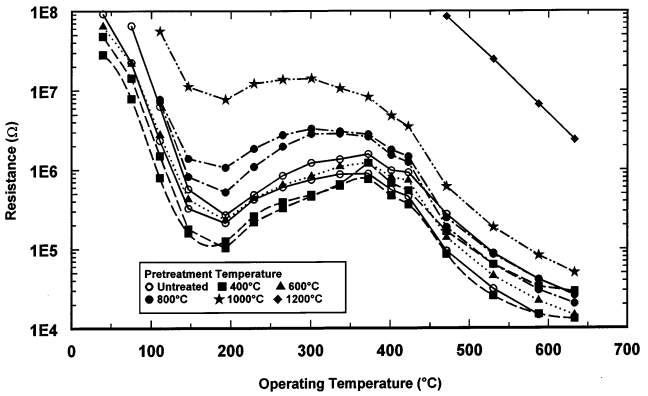

Fig. 14. Dry air baseline resistances of variously pretreated n-SnO_2 disc samples as a function of operating temperature.

effect of variations in CH_4 concentration upon sensitivity at an operating temperature of 617°C, the air baseline resistances were significantly greater than previously observed, although the sensitivities around 1000 ppm were broadly comparable with earlier data (see Table 5). The sensitivity increased monotonically with gas concentration, although the data across the concentration range were not well described by a single power law relationship as indicated by the non-linear characteristics in Fig. 19.

4. Discussion

4.1. Physical parameters of samples

The thermal treatment of nanopowders creates aggregates of varying sizes composed of nanoparticles of relatively uniform size. The pore space within these assemblages is the microporosity which is associated with the high pressure region of the intrusion/retraction curves. Narrow throat-radius and chamber-radius distributions are therefore expected for all samples (component distribution 1 in Figs. 7–12 and Table 1). The actual throat size distributions are expected to be somewhat broader than those reported here due to network connectivity effects [7,23], although the mean values are considered accurate. In contrast, the actual chamber-radius distributions are expected to have larger mean values and standard deviations than implied by Figs. 7–12 because of the permanent entrapment of mercury in large chambers during retraction [7].

The macroporosity is the pore space left between aggregates and is associated with the low pressure region of the mercury/retraction curves. Pore-network simulation studies of mercury porosimetry [7–9,23] have shown that the large width of mercury intrusion curves may indicate: (a) weak connectivity of the pore network; (b) strong correlation between chamber and throat sizes; and (c) significant fractal roughness porosity. Assuming that compression of powders yields aggregates of a great variety of sizes, then their clustering can give rise to strong spatial correlation between pore sizes. The fractal roughness porosity is attributed to the pendular rings formed in regions where the aggregates touch each other. Hence, the modest gradient in the low pressure part of the mercury intrusion curves is due to the small-scale heterogeneities of macroporosity (that is, spatial pore size correlation) and the significant fraction of toroidal pore volume that is filled with mercury over a wide pressure region [5]. Based on previous experience with simulation studies [8], it can be assumed that the larger of the two component throat-size distributions (component distribution 2 in Table 1 and Figs. 7–12) is a good approximation to the actual one, because of the existence of spatial pore size correlations. However, it widens and shifts to smaller sizes because of the existence of pendular rings at grain contacts [5].

The monotonic loss in surface area with increasing sample pretreatment temperature has been previously noted in SnO_2 produced via different routes [24]. Initially, this appears to be achieved without any major variation in pore diameter or mean particle size, but for material presintered above 600°C, there is clear evidence for grain growth. The colour differences between the samples are consistent with gradual elimination of SnO with increasing pretreatment temperature in air [2], i.e. a change in the nonstoichiometry of the oxide represented by x in the formula SnO_{2-x}.

For discs pretreated at 400°C upwards, the decrease in surface area is accompanied by an increase in the mean pore diameter, whilst the porosity appears to reach a maximum in samples pretreated at 800°C. Untreated discs have porosities, pore volumes and mean pore sizes similar to those of samples fired at 600–800°C, although the specific surface area was higher than that of any other material. The unpressed precursor powders show a very similar trend in terms of surface area, but retain greater porosity and pore volume at any given pretreatment temperature because they have not been subjected to the high compression pressures involved in disc fabrication.

4.2. Electrical behaviour in air

The sigmoid air resistance behaviour of fresh SnO_2 discs has been reported previously [1,2] and shows a clear trend with pretreatment temperature. However, it is apparent from Fig. 14 that the operating temperature is generally of greater significance in determining the air resistance. There is no evidence to suggest that the contact curing process has a significant effect upon the subsequent air resistance behaviour of samples.

Table 2
Estimated mean air baseline resistances and activation energies for variously pretreated n-SnO_2 pressed disc samples in dry air

	Estimated air resistance (Ω)		Estimated activation energy (eV)	
Operating temperature (°C)	~120	~340	20→150	350→800
Pretreatment temperature (°C)				
Untreated	4.56e+06	8.92e+05	−0.72	−0.94
400	1.14e+06	7.15e+05	−0.58	−0.78
600	2.65e+06	1.16e+06	−0.50	−0.87
800	9.75e+06	2.36e+06	−0.82	−0.99
1000	6.23e+07	9.59e+06	−0.86	−1.02
1200	>1e+08	>1e+08	–	−1.23

Activation energy analyses have been used by other workers [24] in attempts to interpret the air resistance behaviour of tin oxide materials produced by different methods. Two of the most commonly-invoked models for the electrical conduction mechanisms in such materials may be summarised as follows [1]:

1. Closed neck intergrain structures where the activation energy is related to surface states associated with the presence of charged species (e.g. O_2^-, O^- or O^{2-}). If the dominant surface species changes from a single to a double charged form, the activation energies in the relevant regions would be expected to differ by a factor of four.
2. Schottky barrier control where the activation energy is related to the barrier height and hence to the square of the surface charge. This model is only expected to produce linear Arrhenius plots in special circumstances and more generally produces sigmoid characteristics.

The activation analysis performed here produced reasonably linear characteristics in the specified operating temperature regions (ambient to 150°C and 350–800°C), tending to support the adoption of model (a). However, the modest increase in E_{Act} between the low and high temperature regions does not indicate a change in the charge of the dominant surface species. By analogy with earlier studies [1,24], it may be suggested that OH^- and (O_2^- or O^-) are likely candidates for the dominant surface species present in air atmospheres which control the sample behaviour in the low- and high-temperature regions respectively. However, such identifications cannot be considered entirely reliable because the experimental conditions (e.g. sample preparation and treatment) undoubtedly affect the empirical values for E_{Act}, as indicated by the range of results quoted in the literature for nominally similar systems [24].

4.3. Electrical behaviour in reducing gases

The peak sensitivities and optimum operating temperatures demonstrated by the pressed disc samples in response to ~1000 ppm of CH_4, CO and H_2 in air are broadly typical of prototype or commercial *n*-type semiconductor sensors comprising sintered pellets of polycrystalline SnO_2 [25]. We also note that significant CO responses at relatively low operating temperatures have been observed elsewhere when using samples of the same type [26], although this aspect of the behaviour has not been examined in detail here. It is clear that the gas sensitivity depends upon operating temperature strongly, whereas much smaller effects are generally attributable to variations in the pretreatment condition. The exception is for samples fired at 1200°C (and, presumably, at higher temperatures), which have negligible sensitivities. The normalised sensitivity ratios in Fig. 18 show similar trends for all three gases and suggest that discs pretreated at 400°C have rather smaller values than either the unfired or 600°C pretreated material.

There is no reason to suggest that models widely used in the literature to describe the behaviour of SnO_2 towards reducing gases at elevated temperatures are not applicable in this case. It may therefore be assumed that the gas responses are predominantly caused by modulations in the net surface coverage of charged oxygen species by reaction with the gas phase reducing species, leading to changes in the charge carrier population within the near-surface layers of the oxide and hence resistance variations in the samples [1,24,25,27].

A striking feature of the data was that unfired samples and those pretreated at temperatures within the operating range (e.g. 400 and 600°C) demonstrated marked differences in baseline resistance and gas sensitivity even after being subjected to operating temperatures at least as great as the firing conditions for several hours. Although the effects of repeated cycling through the operating temperature range were not studied in detail, observations provided no strong evidence for rapid convergence of sample properties in these circumstances. For example, data in Table 5 were obtained from samples undergoing their third excursion to operating temperatures in excess of 600°C. Nevertheless, clear trends in the baseline resistance and gas sensitivity behaviour as a function of pretreatment condition are

Table 3
Mean gas sensitivities of variously pretreated n-SnO_2 pressed disc samples

	Pretreatment temperature (°C)					
Operating temperature (°C)	Untreated	400	600	800	1000	1200
1097 ppm CH_4						
131	0.21	−0.40	−0.10	−0.01	0.06	–
174	−0.05	0.01	−0.10	−0.10	−0.04	–
227	−0.14	−0.06	−0.06	−0.13	0.00	–
258	0.25	0.25	0.19	0.24	0.20	–
301	0.04	−0.29	0.09	0.02	0.11	–
339	0.39	0.43	0.56	0.47	0.40	–
409	4.92	1.85	2.21	2.56	1.65	–
420	2.52	3.18	3.41	3.22	1.78	–
497	7.80	7.04	9.12	7.68	5.14	–
530	9.92	9.24	7.96	7.27	6.29	0.05
533	8.21	5.55	8.72	6.94	5.28	0.00
603	7.31	3.90	7.26	5.64	5.05	0.15
647	3.09	7.03	4.19	3.04	2.96	0.17
678	3.61	1.99	3.40	3.02	2.31	0.23
733	1.06	2.53	1.66	1.08	1.23	0.08
739	1.85	1.13	1.75	1.66	–	0.19
785	1.10	0.68	1.09	1.00	0.71	0.16
1000 ppm CO						
131	6.8	3.0	2.1	2.0	1.6	–
174	10.5	5.9	2.6	3.1	1.8	–
227	8.6	9.4	4.4	5.9	1.5	–
258	6.0	4.6	15.5	6.5	8.1	–
301	6.1	7.2	5.0	6.1	4.2	–
339	15.8	14.9	24.4	16.9	16.6	–
420	29.5	27.2	36.9	31.1	30.9	–
497	8.9	6.2	6.3	5.7	12.3	–
530	1.2	3.5	−1.0	−0.1	0.4	1.4
533	3.5	2.0	2.3	1.9	4.1	0.0
603	1.5	1.3	1.1	0.9	2.2	1.5
647	0.1	1.3	0.3	0.2	0.2	1.3
678	0.4	0.5	0.3	0.3	0.2	0.2
733	0.0	0.3	0.2	0.1	0.1	0.5
739	1.3	1.1	1.2	1.2	–	2.8
785	0.2	0.1	0.2	0.2	0.2	0.1
1000 ppm H_2						
131	−0.8	−0.7	−0.8	−0.6	−0.7	–
174	6.0	0.3	0.3	0.5	0.3	–
227	26.2	20.7	12.8	15.7	10.9	–
258	9.8	9.5	16.8	11.0	11.2	–
301	43.8	40.3	35.7	40.4	35.0	–
339	30.3	26.8	44.8	27.5	31.6	–
409	71.2	–	61.6	61.1	49.5	–
420	51.7	39.6	53.0	43.4	39.8	–
497	27.0	17.3	18.8	17.8	48.4	–
530	5.5	29.8	9.6	6.5	8.1	2.6
533	10.5	6.3	7.0	6.9	11.0	0.0
603	3.3	3.2	2.4	2.2	5.1	1.3
647	0.7	4.0	1.2	0.6	0.9	1.9
678	1.1	1.5	0.9	0.8	0.7	0.5
733	0.3	2.9	0.5	0.3	0.4	0.8
739	2.2	2.0	2.0	1.9	–	3.6
785	0.3	0.3	0.3	0.3	0.4	0.1

apparent. It is difficult at this stage to provide a clear explanation for this effect, other than to hypothesise that the initial treatment produces material properties which subsequently require much more severe conditions to induce further changes than employed in these experiments. This may be related to the rate of quench-

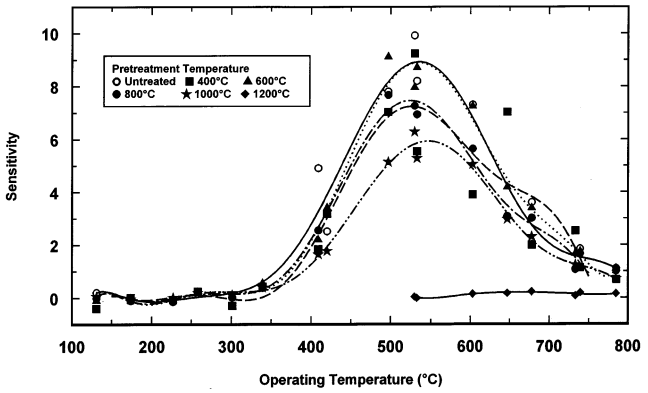

Fig. 15. Sensitivity of variously pretreated n-SnO_2 disc samples to 1097 ppm CH_4 in dry air as a function of operating temperature.

ing at the end of the firing period, which is likely to be more rapid than that experienced by samples undergoing gas tests.

4.4. Correlation of physical and electrical properties

The mean baseline ratio distribution (Fig. 18) is well correlated with the rapid growth in particle size and pore diameter and the reduction in surface area (Fig. 13) as a function of pretreatment temperature. However, it is well known that reduced nonstoichiometry of SnO_{2-x} resulting from elimination of oxygen vacancies during sintering in air leads to higher intrinsic resistances [24] and the important role of the dominant surface chemical species in controlling the baseline resistance have already been discussed. Consequently, there does not appear to be a strong basis on which to propose a direct causal link between these effects.

The gas sensitivity ratios (Fig. 18) also demonstrate a good correlation with parameters which describe the pore structure of the oxide as a function of pretreatment temperature. In particular, the porosity and pore volume (Fig. 13) show similar distributions for samples pretreated at temperatures below 1200°C, most notably

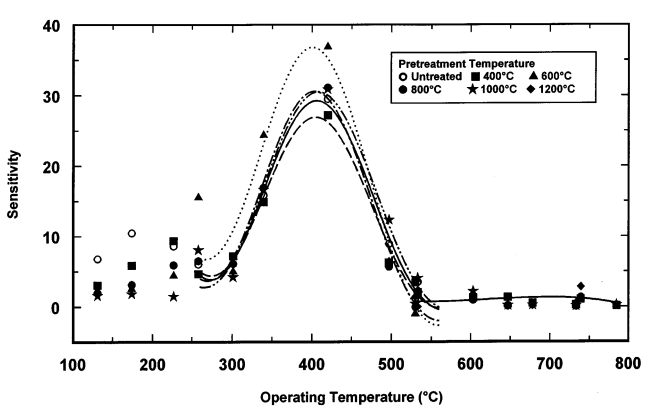

Fig. 16. Sensitivity of variously pretreated n-SnO_2 disc samples to 1000 ppm CO in dry air as a function of operating temperature.

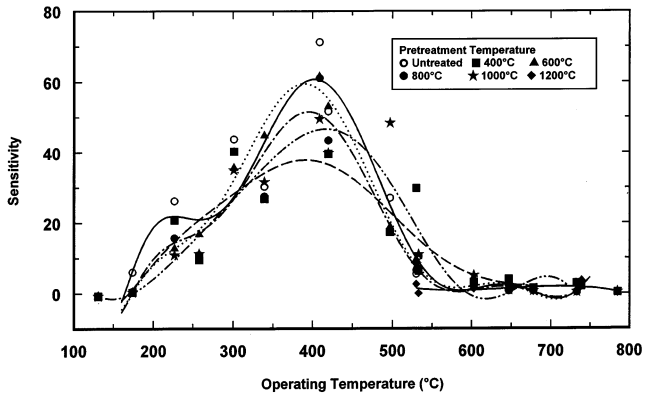

Fig. 17. Sensitivity of variously pretreated n-SnO_2 disc samples to 1097 ppm H_2 in dry air as a function of operating temperature.

the dip at 400°C. The agreement is less marked at the highest pretreatment temperatures where the gas sensitivity declines very rapidly despite the retention of significant porosity. Fig. 8(a) indicates that firing the pressed discs at 400°C eliminates the larger of the two component distributions of the throat size found in the untreated sample case (Fig. 7(a)). In combination with the fact that the larger component chamber size distribution also shifts to lower values, this is expected to have a strong negative effect on the diffusivity in the pore structure. Further increase in the treatment temperature partially restores the larger component throat size distribution and significantly increases the mean chamber size. The observation that the gas sensitivities also exhibit a minimum also at this pretreatment temperature may imply that the overall sensing process is controlled by diffusional limitations in these samples. This is probably not the case at significantly higher sintering temperatures where a collapse in the specific surface area and a very rapid increase in the mean pore sizes is observed. These oxide samples are more likely to demonstrate sensing behaviour that is limited by the availability of surface sorption and reaction sites.

The preceding comments are subject to the qualification that in both regimes the operating temperature of the sample exerts a dominant effect upon the observed sensitivity for all samples except those pretreated at the highest temperatures. This can be understood by appreciating that the diffusion of reactant and product species through material under porosity control is still a sensitive function of temperature. Based on the pore size distribution results of this work, both Knudsen and ordinary molecular diffusion mechanisms appear to control the molecular transport through the pore structure of the ceramic. The diffusivities in these two regimes are strongly non-linear functions of the absolute temperature, T: the Knudsen diffusivity increases as $T^{1/2}$ whereas the bulk diffusivity increases as $T^{3/2}$. Similarly, in a sample where surface chemistry is the controlling factor, the thermodynamic effects of operating temperature upon sticking coefficients and reaction

Table 4
Results of air baseline and gas sensitivity data analyses for variously pretreated n-SnO_2 pressed disc samples

Pretreatment temperature (°C)	Untreated	400	600	800	1000	1200
Mean baseline ratio (%)	1.0×10^2	$(6.2 \pm 3.0) \times 10^1$	$(9.0 \pm 2.0) \times 10^1$	$(2.24 \pm 0.87) \times 10^2$	$(1.21 \pm 0.95) \times 10^3$	$(3.1 \pm 1.3) \times 10^4$
Methane (1097 ppm)						
Peak operating temperature (°C)	539	529	539	524	550	~650
Sensitivity maximum	8.9	7.3	8.9	7.5	5.9	~0.1
Mean sensitivity ratio (%)	100	81.8	99.6	84.2	66.6	1.1
Carbon monoxide (1000 ppm)						
Peak operating temperature (°C)	405	407	400	406	410	~700
Sensitivity maximum	29.3	27.1	37.0	30.8	30.6	~0.0
Mean sensitivity ratio (%)	100	92.5	126.3	105.1	104.4	~0.0
Hydrogen (1000 ppm)						
Peak operating temperature (°C)	404	395	391	398	417	~700
Sensitivity maximum	61.4	38.4	59.5	51.9	46.9	~2.0
Mean sensitivity ratio (%)	100	62.5	96.9	84.5	76.4	~3.3

probabilities are expected to exert a dominant influence upon the observed behaviour. The study of the correlation of diffusion and surface chemistry with the porosity and gas sensing properties of the SnO_2 samples examined here is already in progress with the aid of molecular simulation techniques.

5. Conclusions

Pressed disc samples fabricated from nanopowder SnO_2 show many characteristics typical of prototype or commercial sensors based on tin (IV) oxide and represent a good basis for comparative gas sensitivity and porosity modelling studies. These in turn can provide information which is of considerable value in the design, fabrication and optimisation of improved gas sensors based on n-SnO_2.

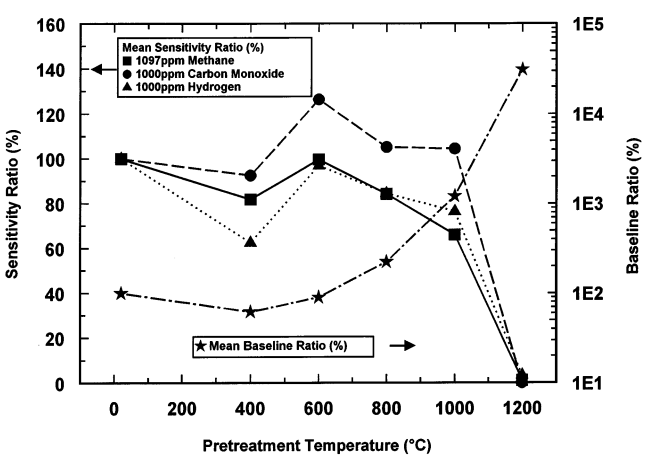

Fig. 18. Mean baseline and sensitivity ratios of variously pretreated n-SnO_2 disc samples (with respect to untreated samples) as a function of pretreatment temperature.

Pretreating in air for 2 h at temperatures between 400 and 1200°C causes particle growth in the oxide which is particularly rapid above 600°C, with a simultaneous reduction in surface area and increase in mean pore diameter. The porosity and pore volume show a local minimum at 400°C and decrease significantly at pretreatment temperatures above 800°C.

Irrespective of pretreatment conditions, the dry air electrical resistance of all samples shows qualitatively similar sigmoid behaviour as a function of operating temperature. Air baseline resistances are more sensitive to operating temperature than to pretreatment temperature although the morphological and compositional changes induced by firing in air exert some influence, especially at the highest pretreatment temperatures. The activation energies in low (<150°C) and high (>350°C) operating temperature ranges do not indicate a difference in the charge of the conductance-controlling surface species in the two regions.

For material pretreated at temperatures below 1200°C, the gas sensitivity strongly depends on operating temperature, with optimum values of 400–530°C depending on species. At the optimum operating temperature, the sensitivity shows a weaker (but nevertheless significant) dependence on pretreatment temperature. There is also a strong correlation between the relative gas sensitivity and the porosity/pore volume parameters of the samples.

It is suggested that in n-SnO_2 subjected to thermal pretreatments resulting in minimal grain growth, the

Table 5
Mean sensitivities of variously pretreated n-SnO_2 pressed disc samples as a function of CH_4 concentration at 617°C

Pretreatment Temperature (°C)	Untreated	400	600	800	1000	1200
Mean baseline resistance (Ω)	1.26e+06	4.02e+06	3.30e+05	3.75e+05	9.71e+05	6.62e+07
Methane concentration (%)	*Gas sensitivity*					
0.005	0.5	0.4	0.4	0.2	0.2	0.1
0.01	1.0	0.5	0.9	0.4	0.4	0.1
0.02	1.6	1.3	1.9	1.1	1.0	0.1
0.03	2.5	0.9	3.4	2.1	1.9	0.1
0.05	3.8	1.7	5.8	4.0	3.4	0.2
0.075	4.4	1.2	6.9	5.0	4.1	0.2
0.1	4.9	1.8	7.8	5.8	4.7	0.3
0.5	8.2	2.5	15.3	12.2	8.9	0.8
1.0	10.0	2.5	19.4	15.7	11.2	1.2
1.5	11.3	2.7	22.4	18.0	12.7	1.4

gas sensitivity is primarily controlled by the effect of operating temperature on the reactant and product diffusion behaviour within the porous oxide structure. Thus, at a fixed operating temperature, the porosity of the material is a key factor in determining the gas response. In more highly sintered materials with large pore structures, surface reaction control is the dominant feature although operating temperature remains the most sensitive modulator of observed sensitivity by virtue of its effect upon the kinetics of gas-surface reactions.

Acknowledgements

This work was performed under Brite Euram contract number BRPR-CT95-0002 supported by the European Commission. The assistance of Dr Hans Ferkel (TUC) and Dr Patrick Keller (FhG-IBMT) in preparing the samples and providing X-ray and SEM analyses is gratefully acknowledged.

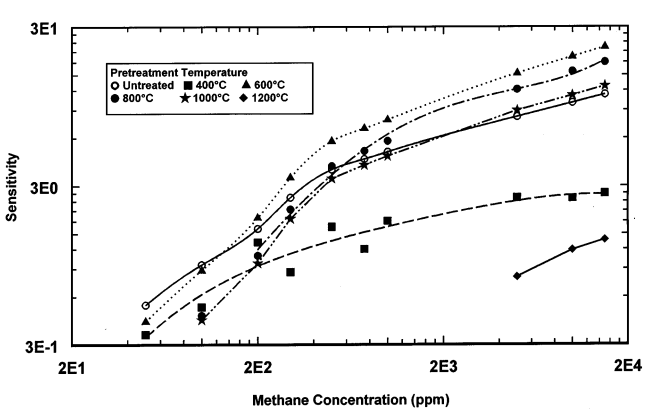

Fig. 19. Sensitivity of variously pretreated n-SnO_2 disc samples to CH_4 in dry air at 617°C as a function of gas concentration.

References

[1] J.F. McAleer, P.T. Moseley, J.O.W. Norris, D.E. Williams, Tin dioxide gas sensors. Part 1–aspects of the surface chemistry revealed by electrical conductance variations, J. Chem. Soc. Faraday Trans. 1 (83) (1987) 1323–1346.
[2] P.G. Harrison, M.J. Willett, Tin oxide surfaces. Part 19—electron microscopy, X-ray diffraction, auger electron and electrical conductance studies of tin (IV) oxide gel and tin oxide surfaces. Part 20—electrical properties of tin (IV) oxide gel: nature of the surface species controlling the electrical conductance in air as a function of temperature, J. Chem. Soc. Faraday Trans. 1 (85) (1989) 1907–1932.
[3] M.J. Willett, Spectroscopy of surface reactions, in: P.T. Moseley, J.O.W. Norris, D.E. Williams (Eds.), Techniques and Mechanisms in Gas Sensing, Adam Hilger, Bristol, 1990, pp. 61–107.
[4] H.H.D. Lee, Validity of using mercury porosimetry to characterize the pore structures of ceramic green compacts, J. Am. Ceram. Soc. 73 (1990) 2309–2315.
[5] R.P. Mayer, R.A. Stowe, Mercury porosimetry: filling of toroidal void volume following breakthrough between packed spheres, J. Phys. Chem. 70 (1966) 3867–3873.
[6] D.M. Smith, D.L. Stermer, Mercury porosimetry: theoretical and experimental characterisation of random microsphere packings, J. Coll. Int. Sci. 111 (1986) 160–168.
[7] C.D. Tsakiroglou, A.C. Payatakes, A new simulator of mercury porosimetry for the characterisation of porous materials, J. Coll. Int. Sci. 137 (1990) 315–339.
[8] C.D. Tsakiroglou, A.C. Payatakes, Effects of pore size correlations on mercury porosimetry curves, J. Coll. Int. Sci. 146 (1991) 479–494.
[9] C.D. Tsakiroglou, A.C. Payatakes, Pore-wall roughness as a fractal surface and theoretical simulation of mercury intrusion/retraction in porous media, J. Coll. Int. Sci. 159 (1993) 287–301.
[10] L.K. Frevel, L.J. Kressley, Modifications in mercury porosimetry, Anal. Chem. 35 (1963) 1492–1502.
[11] R.P. Mayer, R.A. Stowe, Mercury porosimetry-breakthrough pressure for penetration between packed spheres, J. Colloid Sci. 20 (1965) 893–911.
[12] F.A.L. Dullien, V.K. Batra, Determination of the structure of porous media, Ind. Eng. Chem. 62 (1970) 25–53.
[13] M. Parlar, Y.C. Yortsos, Percolation theory of vapor adsorption-desorption processes in porous materials, J. Coll. Int. Sci. 124 (1988) 162–176.

[14] H. Liu, L. Zhang, N.A. Seaton, Analysis of sorption hysteresis in mesoporous solids using a pore network model, J. Coll. Int. Sci. 156 (1993) 285–293.
[15] C.A. Jessop, S.M. Riddiford, N.A. Seaton, J.P.R.B. Walton, N. Quirke, The determination of the pore size distribution of porous solids using a molecular model to interpret nitrogen adsorption measurements, in: Rodriguez-Reinoso, et al. (Eds.), Proceedings of the IUPAC Symposium on Characterisation of Porous Solids COPS-II, Alicante, Spain, 6–9 May 1990, Elsevier, Amsterdam, 1991, pp. 123–132.
[16] M. Miyahara, T. Yoshioka, M. Okazaki, Observation of interface curvature of capillary condensed phase in slit-shaped nano pores with a new MD simulation method, in: McEaney et al. (Eds.), Proceedings of the IUPAC Symposium on Characterisation of Porous Solids, COPS-IV, University of Bath, UK, 15–18 September 1996, The Royal Society of Chemistry, 1997, pp. 283–290.
[17] B. Sahouli, S. Blacher, F. Brouers, Fractal analysis of aerogels and carbon blacks using nitrogen adsorption data: comparative study of two methods, in: McEaney et al. (Eds.), Proceedings of the IUPAC Symposium on Characterisation of Porous Solids, COPS-IV, University of Bath, UK, 15–18 September 1996, The Royal Society of Chemistry, 1997, pp. 283–290.
[18] H. Ferkel, J. Naser, W. Riehemann, B.L. Mordike, Production of nanoscaled metal oxide particles by laser evaporation of solids, in: J. Schwedes, S. Bernodat (Eds.), Fine Solid Particles, Shaker, Aachen, 1997, pp. 144–151.
[19] R.W. Smithwick, Compression equations for mercury porosimetry, Powder Technol. 33 (1982) 55–64.
[20] R.W. Smithwick, Contact-angle studies of microscopic mercury droplets in glass, J. Coll. Int. Sci. 123 (1988) 482–485.
[21] L.C. Drake, H.L. Ritter, Macropore-size distributions in some typical porous substances, Ind. Chem. Eng. (Anal. Ed.) 17 (1945) 787–791.
[22] Y. Bard, Nonlinear Parameter Estimation, Academic Press, New York, 1974.
[23] C.D. Tsakiroglou, A.C. Payatakes, A new mercury intrusion-retraction simulator used as a means for the characterisation of porous materials, in: Rodriguez-Reinoso, et al. (Eds.), Proceedings of the IUPAC Symposium on Characterisation of Porous Solids COPS-II, Alicante, Spain, 6–9 May 1990, Elsevier, Amsterdam, 1991, pp. 169–178.
[24] M.J. Willett, Tin (IV) oxide gas sensors: surface chemistry and electrical conductance effects, Ph.D. Thesis, University Of Nottingham (1987).
[25] K. Ihokura, J. Watson, The Stannic Oxide Gas Sensor: Principles And Applications, CRC Press, Boca Raton FL, 1994.
[26] G.E. Williams, The gas sensing properties of nanocrystalline powders produced by a laser evaporation route, J. Mater. Chem. (1998) in press.
[27] D.E. Williams, Conduction and gas response of semiconductor gas sensors, in: P.T. Moseley, B.C. Tofield (Eds.), Solid State Gas Sensors, Adam Hilger, Bristol, 1987, pp. 71–123.

Biographies

Martin J. Willett obtained a B.Sc. degree in physics from Birmingham University in 1978 and a Ph.D. in chemistry from Nottingham University in 1987 for work on the surface chemistry of semiconductor gas sensors. From 1978 until 1994 he worked in the Technical Services and Research Executive of the British Coal Corporation. His major contributions were in the development of improved sensors for the detection of gases in underground coal mines using diverse technologies including catalytic, electrochemical, semiconductor and optical methods. He also helped to develop and successfully demonstrate a ruggedised distributed optical fibre temperature sensor for the detection of spontaneous combustion in underground mines. In 1994 he joined City Technology Ltd, the world's largest independent supplier of gas sensors, where he is the Research Manager. His active research interests include the development of improved electrochemical and potentiometric sensors, investigations into novel catalytic sensor design concepts and the application of optical techniques in stable, low cost sensors.

Vasilis N. Burganos received his diploma in Chemical Engineering from the National Technical University, Athens, in 1983 and his Ph.D. from the University of Rochester, USA, in 1988. His postgraduate research involved the modelling and simulation of gas diffusion in random pore structures using network models and Monte Carlo techniques. In 1988 he joined ICE-HT/FORTH as a Research Associate and participated in a number of European Union projects dealing with multiphase flow and diffusion in porous solids. In 1994 he became Principal Researcher at ICE-HT/FORTH. His research interests include diffusion and sorption in porous materials, single and multiphase flow in porous media, separation processes, pore structural analysis, conduction in random media, land contamination, industrial furnace operation, capillarity, jet-break up and atomisation, non-equilibrium thermodynamics, molecular simulations, lattice fluids, numerical techniques for engineering applications.

Christos D. Tsakiroglou received his diploma in Chemical Engineering from the Aristotle University of Thessaloniki in 1985 and his Ph.D. degree from the University of Patras in 1990. His postgraduate research involved the development of improved techniques for the characterisation of the microstructure of porous materials. He participated in projects at ICE/HT-FORTH as a Research Associate until 1994. He then spent 1 year as a post-doctoral Research Fellow at Institut Francais du Petrole, France, before rejoining ICE/HT-FORTH in 1995. His research interests include characterisation of porous materials, multiphase flow in porous media, capillary and electrical properties of porous media, soil pollution and remediation, formation of dioxins and furans in incinerators and cement kilns.

Alkiviades C. Payatakes received his Dipl. Ing., Chemical Engineering,, from the National Technical University, Athens, in 1968 and his Ph.D. from Syracuse University, USA, in 1973. His postgraduate research involved the experimental and theoretical analysis of

depth filtration. In 1974 he joined the Dept. of Chemical Engineering of the University of Houston where he reached the rank of Full Professor in 1980. In 1981 he joined the Dept. of Chemical Engineering of the University of Patras, Greece. Since 1984 he has also been a Researcher at ICE-HT/FORTH. His research interests include multiphase transport phenomena in porous media and in particulate systems, characterisation of porous materials, depth filtration, physicochemical hydrodynamics, simulation of fluid and interface flow using cellular automata, behaviour of organic pollutants in soils including natural attenuation, clean combustion, combustion gas sensors, development of new instruments.